



UNIVERSITY OF LEEDS

This is a repository copy of *Atom probe tomography analysis of the reference zircon gj-1: An interlaboratory study*.

White Rose Research Online URL for this paper:
<http://eprints.whiterose.ac.uk/137226/>

Version: Accepted Version

Article:

Exertier, F, La Fontaine, A, Corcoran, C et al. (23 more authors) (2018) Atom probe tomography analysis of the reference zircon gj-1: An interlaboratory study. *Chemical Geology*, 495. pp. 27-35. ISSN 0009-2541

<https://doi.org/10.1016/j.chemgeo.2018.07.031>

© 2018 Elsevier B.V. Licensed under the Creative Commons Attribution-NonCommercial-NoDerivatives 4.0 International License (<http://creativecommons.org/licenses/by-nc-nd/4.0/>).

Reuse

This article is distributed under the terms of the Creative Commons Attribution-NonCommercial-NoDeriv (CC BY-NC-ND) licence. This licence only allows you to download this work and share it with others as long as you credit the authors, but you can't change the article in any way or use it commercially. More information and the full terms of the licence here: <https://creativecommons.org/licenses/>

Takedown

If you consider content in White Rose Research Online to be in breach of UK law, please notify us by emailing eprints@whiterose.ac.uk including the URL of the record and the reason for the withdrawal request.



eprints@whiterose.ac.uk
<https://eprints.whiterose.ac.uk/>

Atom probe tomography analysis of the reference Zircon GJ-1: a round-robin experiment

A. La Fontaine^{1,2,*}, F. Exertier^{1,2}, C. Corcoran³, S. Piazzolo^{3,4}, E. Belousova⁴, Z. Peng⁵, B. Gault⁵, D. W. Saxey⁶, D. Fougereuse⁶, S. M. Reddy⁶, S. Pedrazzini⁷, P. A. J. Bagot⁸, M. P. Moody⁸, B. Langelier⁹, D.E. Moser¹⁰, G.A. Botton⁹, F. Vogel¹¹, G.B. Thomson¹¹, P.T. Blanchard¹², A.N. Chiaramonti¹², D.A. Reinhard¹³, K.P. Rice¹³, D. Schreiber¹⁴, K. Kruska¹⁴, W. Jing¹⁴, J. M. Cairney^{1,2}

¹School of Aerospace, Mechanical, Mechatronics Engineering, University of Sydney, NSW 2006, Australia

²Australian Centre for Microscopy and Microanalysis, University of Sydney, NSW 2006, Australia

³Australian Research Council and Centre of Excellence for Core to Crust Fluid Systems / GEMOC, Department of Earth and Planetary Sciences, Macquarie University, NSW 2109, Australia

⁴School of Earth and Environment, University of Leeds, UK

⁵Max-Planck-Institut für Eisenforschung GmbH, Max-Planck-Straße 1, 40237 Düsseldorf, Germany

⁶Geoscience Atom Probe, Advanced Resource Characterisation Facility, John de Laeter Centre, Curtin University, WA, 6102, Australia

⁷Department of Materials Science and Metallurgy, University of Cambridge, Cambridge CB3 0F3, UK

⁸Department of Materials Science, University of Oxford, Parks Road, Oxford, OX1 3PH, UK

⁹Department of Materials Science and Engineering, and Canadian Centre for Electron Microscopy, McMaster University, 1280 Main Street West, Hamilton, ON, L8S 4M1, Canada

¹⁰Department of Earth Sciences, University of Western Ontario, 1151 Richmond Street, London, ON, N6A 5B7, Canada

¹¹Department of Metallurgical & Materials Engineering, University of Alabama, Tuscaloosa, AL 35401

¹²National Institute of Standards and Technology, NIST Boulder, U.S. Department of Commerce

¹³CAMECA Instruments, Inc., 5470 Nobel Dr, Madison, WI 53711

¹⁴Pacific Northwest National Laboratory, MSIN J4-55 Richland, WA 99352 USA

*corresponding author: A. La Fontaine, alex.lafontaine@sydney.edu.au

ABSTRACT

In recent years, atom probe tomography (APT) has been increasingly used to study minerals, and in particular Zircons. The mineral Zircon (ZrSiO_4) is ideally suited for geochronology by utilising the U-Th-Pb isotope systems, and trace element compositions are also widely used to constrain petrogenetic processes. However, while standard geoanalytical techniques provide information at micron scale lengths, the unique combination of chemical/isotopic sensitivity and spatial resolution of APT allows compositional measurements at the nanoscale. This round robin study is aimed at understanding the reproducibility of APT data across research facilities

and assessing the role of different aspects of the atom probe workflow on reproducibility. This is essential to allow correct evaluation of APT results and full utilization of this emerging technique within the geoscience community. In this study, nine samples from the same GJ-1/87 grain were sent to nine APT institutes in Europe, USA, Canada and Australia. Each institute conducted three different rounds of APT analyses: using (i) unconstrained analysis parameters, [1] pre-defined analysis parameters, and (iii) a data analysis exercise. Data such as the measured composition, acquisition parameters, or mass spectrum peak identifications, were recorded and analyzed. We observe a significant variation in the measured composition across this round robin study as well as the number of trace elements identified. These differences are thought to directly result from the user's choice of peak identification, ranging and background correction model. The type of instrument does not seem to be a critical factor.

Consequently, comparison of absolute trace element data on zircon using APT between laboratories is only valid if the same workflow has been ensured.

KEY WORDS

Round robin; Atom probe tomography; zircon

1. INTRODUCTION

The accessory mineral zircon (ZrSiO_4) is commonly used in geoscience as a geochronometer utilising the U-Th-Pb isotope systems and also as a trace element monitor. This is essentially due to its ability to specifically incorporate very specific trace elements such as U and Th, but exclude Pb during crystallization as well as the robustness of its lattice structure, composed of isolated SiO_4 tetrahedra, which leads to refractory and weather-resistant properties. [2, 3] The extremely slow diffusivity of solutes, even at high temperature, and the homogeneity of trace element distribution, both contribute to zircon's use as a "recording system". [4-6]

Laser ablation inductively coupled mass spectrometry (LA-ICPMS) is commonly used to measure the trace element composition in zircons because of its high chemical sensitivity, despite a spatial resolution limited to $\sim 10 \mu\text{m}$. [7] In the last decade, studies using advanced electron microscopy, cathodoluminescence and secondary ion mass spectrometry showed that trace elements can be heterogeneously distributed within zircons at the micrometer and sub-micrometer scale, principally in domains affected by crystal-plastic deformations. [8-14] Trace element mobility is also observed in old zircons with high Uranium content due to radiation damage. [15] In order to better understand the processes responsible for such heterogeneities

and trace element mobility, the geoscience community requires techniques that combine sub-micrometer spatial resolution with high chemical sensitivity. For example, high-resolution ion microprobe (nano-SIMS) can reach a lateral resolution as small as to 50 nm while maintaining a high chemical sensitivity, usually below 1 ppm. [16-18] In parallel, atom probe tomography (APT) has recently emerged as a technique providing three-dimensional, subnanometer-scale analysis of minerals with a unique combination of chemical/isotopic sensitivity and near-atomic resolution. [19, 20] In recent years, APT has been increasingly applied to the study of trace element distribution in zircons. [21-25]

APT relies on the effect of an intense electric field generated at the tip of a 50-100 nm diameter needle-shaped specimen biased to a high voltage, in the range of 3–11kV. As this electrostatic field reaches a critical value in the range of 10^{10} – 10^{11} Vm^{-1} , the surface atoms are progressively ionized and desorbed from the surface in a process known as field evaporation. Upon laser-assisted field evaporation, the ions are accelerated away from the specimen and projected onto a position-sensitive detector, with a magnification that routinely reaches 10^6 x. Field evaporation is a thermally-assisted process, critically dependent on the amplitude of the electric field. Time-control of the field evaporation process is gained by superimposing laser pulses to the DC voltage, allowing for time-of-flight mass spectrometry with unrivalled spatial resolution. Modern atom probe microscopes are of two main types, with some fitted with a reflectron lens, which acts as an electrostatic mirror that modifies the flight path of ions having different kinetic energies to improve the mass resolution, while maintaining the field-of-view. [26, 27]

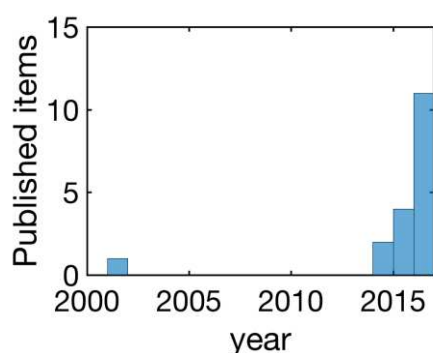


Figure 1: publications on atom probe applied to geological materials 2000-2016.

After some early attempts [28, 29], improvements in APT instrumentation and specimen preparation methods have supported a rising interest by the geoscience community in recent years [22-25, 30], as evidenced by the number of published documents reported in

Figure 1. Hence, it is timely for the APT community to evaluate the reproducibility of the technique on well-characterized, standard geological materials. It has been widely reported that the composition measured by APT is dependent on the analysis conditions, namely the base temperature, the pulsing mode (high-voltage vs. laser), the laser pulse energy, the amplitude of the DC field, detection rate, the type of instrument and detector used. [31-41]. In order to monitor experimental biases and results reproducibility, the geoscience community relies on stable and homogenous reference zircons that have enabled routine compositional analysis using LA-ICPMS [42]. One such reference zircon (GJ-1) was developed by the ARC National Key Centre for Geochemical Evolution and Metallogeny of Continents (GEMOC) and the ARC Centre of Excellence for Core to Crust Fluid Systems (CoE/CCFS) at Macquarie University in Australia. In recent years, it has been widely distributed and used as a chemical reference material for zircon U-Pb geochronology and Hf-isotope analysis. [43]

Here, we report on a round-robin APT experiment making use of one grain of this reference zircon GJ-1. To date, only few round-robin experiments in APT have been reported in the open literature [44, 45], but the community is increasingly using this approach to assess analysis methods and techniques. For example, testing the reliability of clustering analysis methods on the same simulated and experimental data sets [1], or the influence of the user on the definition of ranges to translate a mass spectrum into an elemental composition [46]. Our effort, coordinated at the University of Sydney, is the first of its kind on a geological material and has utilised nine state-of-the-art instruments spread across Europe, Canada, USA and Australia. Fragments from the same zircon GJ-1 grain (grain # 87) were cut and sent to the different laboratories for analysis. The round-robin consisted of 3 different rounds of analysis: (i) unconstrained acquisition parameters and data processing; (ii) pre-defined acquisition parameters, and (iii) data processing solely, on a constrained dataset. Here we present the results from this round robin experiment, namely, recording the acquisition parameters, the quality of the mass spectra, the identification of peaks in the mass spectrum, and the subsequent measurement of the composition, for the primary and trace elements. From our analysis, we derive the critical parameters and lay out what could become best practice in the field.

2. EXPERIMENTAL PROCEDURE

2.1 Round robin experiments

This round robin study was set up as a collaboration between nine APT laboratories in five different countries equipped with four different models of commercial Local Electrode Atom Probes (CAMECA LEAP[®]), all equipped with UV ($\lambda=355\text{nm}$) laser systems as summarized in Table 1. The single grain of reference zircon was obtained from GEMOC/CCFS at Macquarie University in Australia.

LEAP 5000XS – Straight Flight Path	3 instruments
LEAP 5000XR – Reflectron	2 instruments
LEAP 4000X HR – Reflectron	3 instruments
LEAP 4000X Si – Straight Flight Path	2 instruments

Table 1: Instruments used in this round robin experiment

Eleven fragments were sectioned from zircon GJ-1/87 to a size of a few mm^2 each. Those samples were given directly to the participants at the Atom Probe Tomography and Microscopy conference in 2016 (APT&M 2016), without providing any information on the sample, except that it was a reference zircon. All participants received a document that defined the protocol of the round robin. The participants were asked to share the results listed in table 2.

Round 1 <i>Unconstrained</i> (Participants collect 1 or more > 20M atoms datasets)	Round 2 <i>Constrained</i> <i>Pre-defined conditions:</i> <i>(300 pJ – 50 K – 250 kHz - 1%)</i> (Participants collected 1 or more > 20M atoms datasets)	Round 3 <i>Ranging</i> (Participants were provided with a 20M atom dataset)
.pos, .epos and .rhit files	.pos, .epos and .rhit files	range file (.rrng,.rng)
reconstruction details	reconstruction details	composition measured
crystal orientation of the tips	range file (.rrng,.rng)	
details of acquisition parameters	composition measured	
range file (.rrng,.rng)		
composition measured		
sample preparation method		

Table 2: Summary of data provided by participants.

2.2 The reference zircon GJ-1/87

The reference zircon used in this study is GJ-1/87 (grain 87): a centimeter size gem quality zircon obtained from GEMOC/CCFS at Macquarie University in Australia. This well-characterized zircon is exceptionally homogeneous from atomic to millimeter scale, as shown in a recent study utilising APT, LA-ICPMS, transmission Kikuchi diffraction (TKD) and electron backscattered diffraction (EBSD). [43] Prior to cutting the samples from the single-crystal GJ-1/87, its homogeneity was evaluated by using EBSD (2a). For EBSD, the zircon grain was mechanically polished and then finished with a colloidal silica-water solution. The sample was then carbon coated. EBSD was performed on a Zeiss EVO scanning electron microscope (SEM) coupled with a HKL NordlysNano high sensitivity EBSD detector and a tungsten source operated at 20 kV. AzTec software (Oxford Instruments) was used to index the EBSD patterns, and the results confirmed that GJ-1/87 is a single grain with no noticeable crystal plastic deformation. The sample was then sectioned using a diamond saw into eleven pieces with a section of approximately 1 mm² and nine of them were given to the participants. In this study, the samples were named with the following convention:

- Number : 4 (LEAP 4000) or 5 (LEAP 5000)
- Letter: R (Reflectron) or S (Straight flight path)
- Roman number: I, II or III for different samples

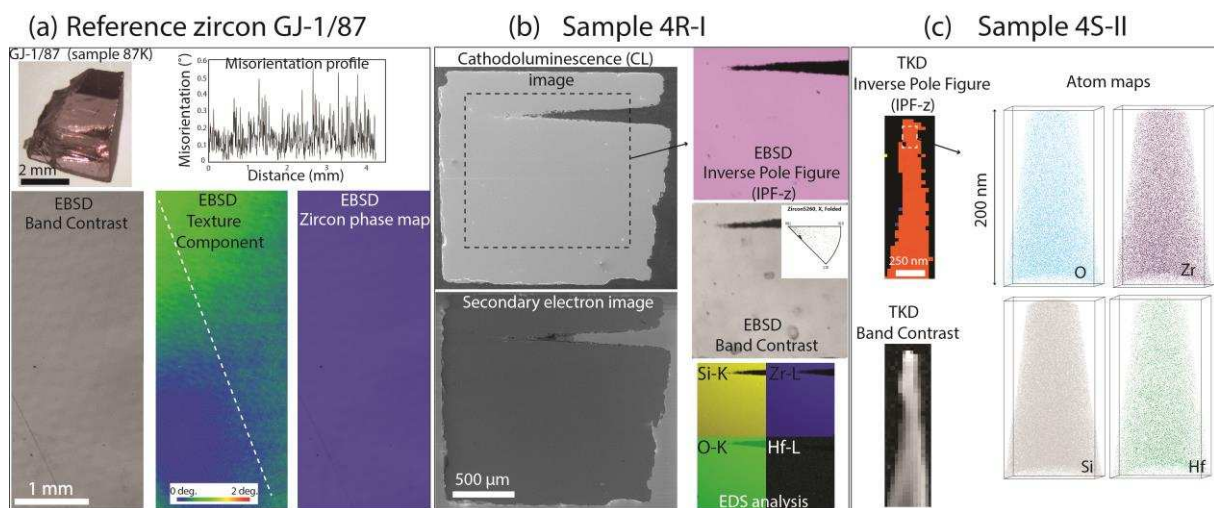


Figure 2: Multi-scale analysis of reference zircon GJ-1/87, confirming absence of structural disturbances and macro-to-nano homogeneity. **(a)** optical image of a small piece from GJ-1/87 (spare piece 87 K) and EBSD analysis of GJ-1/87 **(b)** Cathodoluminescence and secondary electron images of sample 4R-I, EBSD and X-ray Energy Dispersive Spectrometry [47] analysis; **(c)** TKD analysis and atom maps of APT specimen needles from sample 4S-II.

Most participants independently performed electron imaging and EBSD analysis. Figure 2b shows images from the SEM and EBSD analyses performed at The University of Sydney (sample piece 4R-I). TKD was also performed on most of the atom probe specimens. TKD analysis on a tip and the associated atom maps from the reconstructed APT dataset is displayed in figure 2c (sample piece 4S-II).

Analysis	Al	P	Ti	Cu	Ga	Ge	As	Rb	Y	Nb	Hf	Ta	Pb	Th	U
Average	5.38	30.5	4.51	0.10	0.45	0.18	0.21	0.06	197	2.01	5535	0.48	76.9	14.1	222
1 σ	0.21	3.0	0.23	0.01	0.02	0.05	0.05	0.01	6.7	0.07	186	0.02	3.3	0.5	8.4

Analysis	La	Ce	Pr	Nd	Sm	Eu	Gd	Tb	Dy	Ho	Er	Tm	Yb	Lu
Average	0.002	15.2	0.03	0.71	1.51	0.89	5.53	1.59	17.3	5.55	23.7	5.46	58.3	8.98
1 σ	0.001	0.64	0.002	0.03	0.06	0.03	0.23	0.05	0.6	0.18	0.83	0.18	2.1	0.30

Table 3: Summary of LA-ICPMS trace element concentrations (ppmw) for the GJ-1/87 zircon standard. (Full data in table S1)

No major cracks or other structural disturbances were observed at the micrometer and sub-micrometer scale in the sample shown. However, we note that one participant reported unusual cracks at the sub-micron scale that complicated the APT specimen preparation and successful analysis. This sample may have been damaged during or after sectioning. The nominal composition of zircon ($ZrSiO_4$) is 66.6 at. % O, 16.6 at. % Zr and 16.6 at. % Si. Trace element concentrations (Table 3) for the GJ-1/87 zircon sample were acquired in-situ using a Photon Machine Analyte Excite Excimer Laser Ablation System (193 nm) attached to an Agilent 7700cx quadrupole inductively coupled plasma mass spectrometer (ICPMS). The working conditions for these analyses were as follows: 5.29 j/cm^2 fluence (or intensity), 50 μm spot size, and a frequency of 5 Hz for the laser pulse rate. The internal standards chosen were CaO for the reference materials (STD610 & BCR2G) and ZrO_2 for the sample analyses.

3. Results and discussion

3.1 Peak identification

Species identification in APT is based on the time-of-flight (TOF) of the field-evaporated ions, converted into a mass-to-charge-state ratio, reported in daltons (Da). The mass-to-charge data is usually represented in a histogram, or ‘mass spectrum’, with peaks in the spectrum corresponding to the detected ions. The shapes of these peaks in APT mass spectra result from time delays in the field evaporation process (laser pulsing), or from a spread in the energy of the emitted ions (HV pulsing), both of which result in a tail in the mass spectrum peaks. [19]

This tail can overlap with other peaks from the same or other elements located at higher mass-to-charge ratios. The background in the mass spectrum is caused by a combination of dark current from the detector, ionization of residual gases from the vacuum chamber by the electrostatic field, and potentially field evaporation of atoms from the specimen thermally activated at the base temperature (generally 20–80 K). A representative mass spectrum is shown in figure 3, and its main features are typical of those acquired from zircons. This mass spectrum was compiled from the sum of all the mass spectra recorded in the unconstrained round and represents over 380 million detected ions.

During the data processing, the user is assisted in a series of automated correction steps by the commercial software package, CAMECA IVASTM, which was used by all participants in the round robin study. For instance, necessary calibration and correction of the measured time-of-flight is performed via application of the methods outlined in [20, 48]. It is performed in a two-step process, successively adjusting the voltage and the flight distance (i.e bowl) corrections for a single mass spectrum peak in order to optimize the peak resolution. These corrections are followed by a mass-to-charge conversion. [20] Here, we are not discussing the influence of those corrections on the overall composition measurements as they are performed blind by all users and are expected to behave in a similar way on all versions of the commercial software used here. We instead focus on the following steps of the data processing, namely the mass spectrum peak identification, ranging and background estimation and correction. The identification of the peaks in the mass spectrum is done manually by the user, who specifies a range of mass-to-charge-state ratios in the mass spectrum to which a specific type of atomic or molecular ion is associated. These mass ranges are one of the key input files in the commercial software package. As shown in Figure 4, four elements were identified consistently by all participants for the three rounds: O, Zr, Si and Hf.

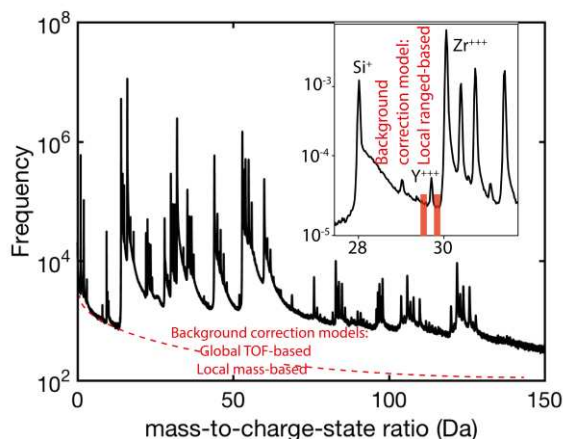


Figure 3: Mass spectrum from zircon GJ-1/87 obtained from the sum of all mass spectra collected in the unconstrained round. Different background correction models highlighted in red.

The majority of participants also identified Y for all rounds. Th, Er and U were identified by two participants and one participant identified more than seven trace elements. The chemical sensitivity of APT is influenced by the position and number of peaks associated with a single element in the mass spectrum, which may include peaks arising from multiple isotopes, molecular ion complexes, and different charge states. In addition, the background level varies across the mass spectral range. In ideal situations, the chemical sensitivity of APT may be below 10 ppma for some elements (Al for example) and as high as hundreds of ppma for others (U for example). The detection of minor trace elements also depends on the size of the dataset. The peaks for some trace elements, such as Th or Er, may be very challenging to quantify with high confidence because they are often similar in magnitude to the local background noise, and may also suffer from isobaric interference or non-detection of their minor isotopes, which can make it difficult to identify them using expected isotopic ratios. It currently falls to the user to decide whether or not to identify and include a peak with a low signal-to-background ratio. In this study, the user choice appeared to be the main factor determining the number of elements identified. There was also no apparent trend between the type of instrument used and the number of peaks identified (Fig. 4).

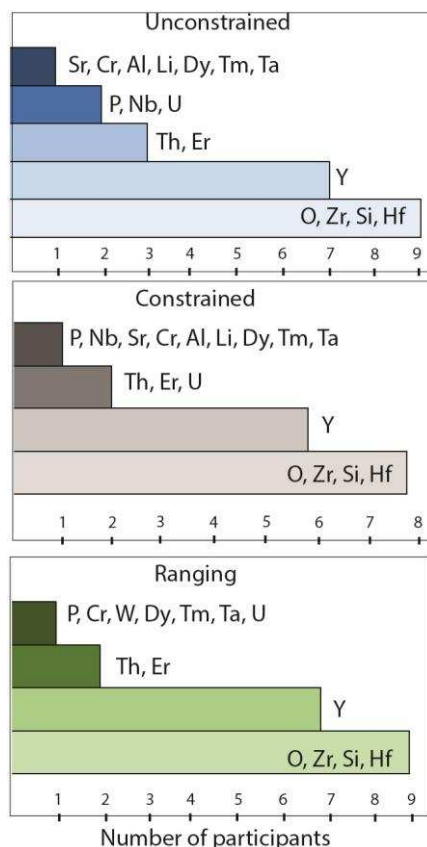


Figure 4: Elements identified in the round robin (excluding C, H and Ga).

The identification of the main elements (O, Zr and Si) and the two main trace elements (Hf and Y; 5535 and 197 ppmw based on LA-ICPMS data) by most of the participants is consistent with previous APT studies of homogeneous zircons in the absence of clustering. [24, 25, 43] (Fig. 4) It is important to note the potential for incorrect ranging in the more detailed trace element analyses, which mostly results from molecular interferences with Zr, Si and O complexes. Essentially, it is up to the participant to push the trace element ranging and confidently address the molecular interferences. In this round robin study, no guidance was given to the participants with respect to data ranging and the difference in participants' geochemistry background is significant, which could explain the distribution observed in the zircon trace element identification.

Figure 5 shows the composition of O, Zr, Si and Hf measured for all three rounds. The full compositions for this study are shown in supplementary tables S3 and S4. The average O content for all rounds (~ 65 at. %) is below its expected nominal composition and its maximum standard deviation for any single round is ~ 3 at. %, which corresponds to that of the unconstrained round .

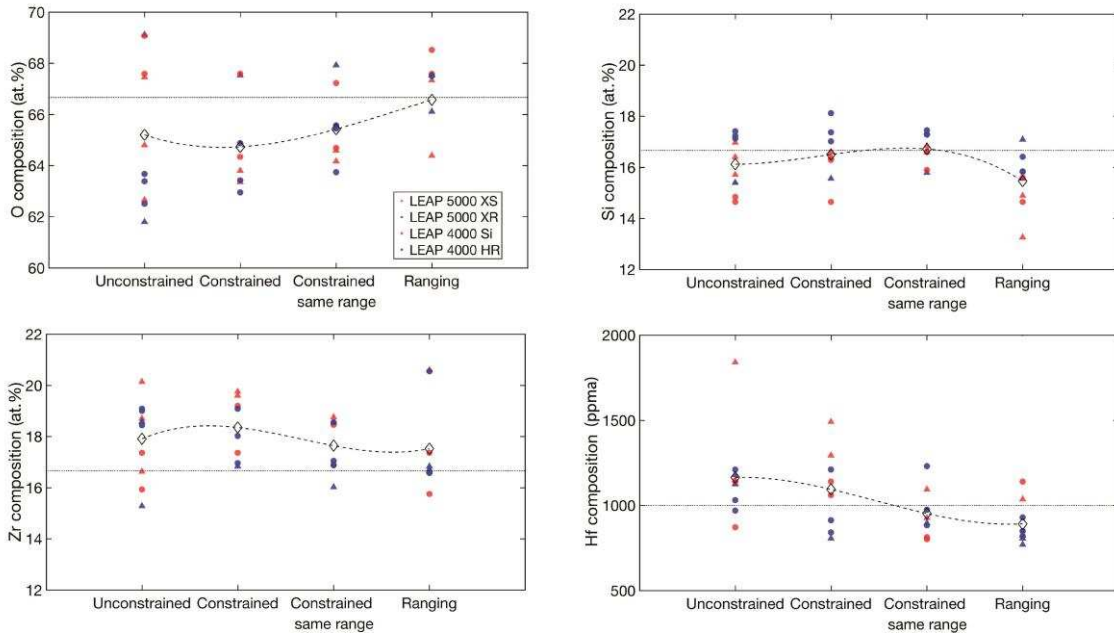


Figure 5: Composition measured for the 4 main elements identified by all participants (O, Zr, Si and Hf) in all rounds. The “constrained same range” data points represent the compositions measured in the constrained round using a prescribed same range that was best fitted to the mass spectra. The average composition is displayed as diamonds. The expected stoichiometric values are also displayed in each case (dashed lines).

The Zr content is consistently overestimated with an average of ~ 18 at.%, while the Si content is closer to its nominal value with an average of ~ 16 at. %. These results are consistent with previous APT studies of zircons, which reported both a deficit of O and a variation in Zr and Si content. [22-25] Hf composition is quite consistent with LA-ICPMS results at around ~ 1000 ppma (~ 5000 ppm).

Figure 5 shows a substantial decrease in the composition value dispersion between the unconstrained and constrained rounds for O and Si. It shows that the different analysis parameters lead, as expected, to a substantial variation in the resulting composition. The harmonization of the ranging and background correction model decrease the deviation in the measured composition even further, as shown in **Figure 5**. The data points corresponding to the ranging round confirm the importance of ranging, and the associated background correction models, by showing a greater variation in measured composition compared to the constrained round using the same range.

3.2 Spectral correction

Once the majority of peaks have been identified and ranged, the background contribution needs to be subtracted in order to obtain an accurate composition. There are three background correction models available in IVAS: (i) global TOF-based which is a background estimate based on the TOF spectrum of the entire dataset that is calculated before reconstruction; (ii) local mass-based correction, which is similar to the global TOF-based estimate but is calculated separately for each mass spectrum created; and (iii) local ranged-assisted background correction, which is calculated for each ranged peak based on the number of counts on either side of the range. [49] The three models are schematically represented in the mass spectrum presented in figure 2.

The data is summarized in supplementary table S2. Seven out of nine participants used the local ranged-assisted background correction. One participant used a background removal method developed in-house, one used the local mass-based correction. The choice of background correction model can be made after the reconstruction.. For complex mass spectra such as those from zircon, the background level varies greatly across the TOF range with the contribution of several, overlapping peak tails. Hence, a more localized evaluation of the background for each peak yields more accurate results. Here, most participants chose the local ranged-assisted background correction, hinting towards a possibility to standardize the background correction model.

3.3 Acquisition and reconstruction parameters

Figure 6 summarizes the principal acquisition parameters used by participants in the unconstrained round. Nearly 20 % of the atom probe data sets were collected with a laser energy of 100 pJ and about 70 % with a laser energy of 400 pJ and below. The majority of participants used an evaporation flux of 1 ion or less per 100 pulses on average, and a specimen base temperature between 45 K and 55 K. The laser pulse frequency varied from 125 kHz to 250 kHz. However, it is irrelevant to compare straight flight path and reflectron-fitted systems in terms of pulse frequency. Often the laser pulse frequency for reflectron-fitted systems is lowered in order to include species with longer times-of-flight..

There is no evident correlation between the acquisition parameters used and the LEAP models (fig. 6). The laser pulse energy is the parameter that varied the most between participants. It is well known that APT data quality is heavily influenced by the laser pulse energy. [35] The choice of laser pulse energy is often guided by the mass spectrum quality, which is usually measured by its background level, thermal tails behind peaks, and mass resolving power. The

data obtained in a typical APT experiment must be reconstructed in order to visualize the 3D volume. Using the simple flight path geometry and the assumption that the specimen is a hemispherical cap on a truncated cone, the ion impact detector coordinates can be used to determine the lateral position of the atoms at the surface of the specimen, and the sequence of evaporation is used to deduce the depth of the atoms within the specimen. The most common APT reconstruction algorithm is based on the work from Bas et al., Geiser et al. and Gault et al. [50-52]. The reconstruction is generally completed with CAMECA's commercial software package IVAS through semi-automated steps where the user can choose to use default parameters or calculate their own reconstruction parameters.

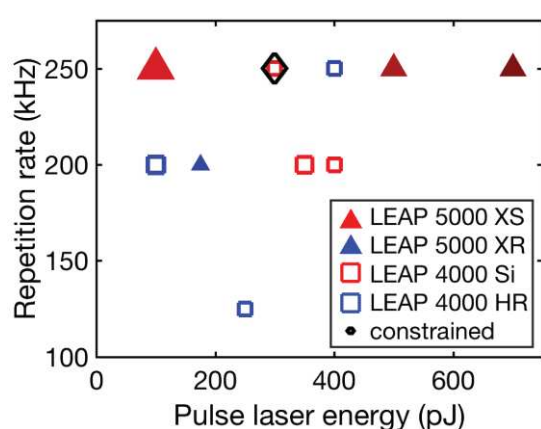


Figure 6: Acquisition parameters used in the unconstrained round: laser pulse energy vs repetition rate. Sample temperature is represented as color brightness (bright 45 K to dark 60 K). Markers are scaled in size according to the detection rates, ranging from 5 ions per 1000 pulses to 2 ions per 100 pulses on average. The black diamond represents the acquisition parameters set in the constrained round. (The full data is reported in Supplementary Table S2)

Optimization of the reconstruction accuracy is widely considered to be a crucial aspect of the APT data processing, as it directly affects the spatial accuracy with which the 3D representation of the field-evaporated volume reflects the true specimen microstructure. In the case we investigate here, where the material is expected to be homogeneous, and we are mainly concerned with composition, the reconstruction step is less critical.

Table S2 shows that the majority of participants calculated their own image compression factor (ICF) and k-factor or used the combination of calculated field evaporation value and atomic volume for Zr. A few participants used the default parameters provided in IVASTM and a single participant used the so-called “tip profile” reconstruction method. [20]

The reconstruction method principally influences the spatial accuracy of the 3d reconstructed volume and has no impact on the time of flight and the composition measured. The zircon GJ-

1/87 sample is perfectly homogenous and as such does not contain any small features that could be used to calibrate the reconstruction, and the nature of zircon field evaporation also does not allow for calibration using crystallographic information. As a result, in this study the spatial accuracy of the 3D volume was not tested.

3.4 Mass spectra and the resulting measured composition

Two close-ups of the mass spectra between 5–26 Da and 40–65 Da collected in both constrained and unconstrained rounds are shown in **Figure 7** (a) and (b) respectively. There are noticeable differences in the background levels and the extent of thermal tails behind major peaks, both of which are influenced by experimental parameters such as the shape of the specimen, the base temperature which influences the thermal diffusivity of the material, the amplitude of the electrostatic field, the laser pulse energy and the instrument vacuum quality. Not all of these factors are easily controllable or reproducible, especially the parameters that are related to the specimen's shape.

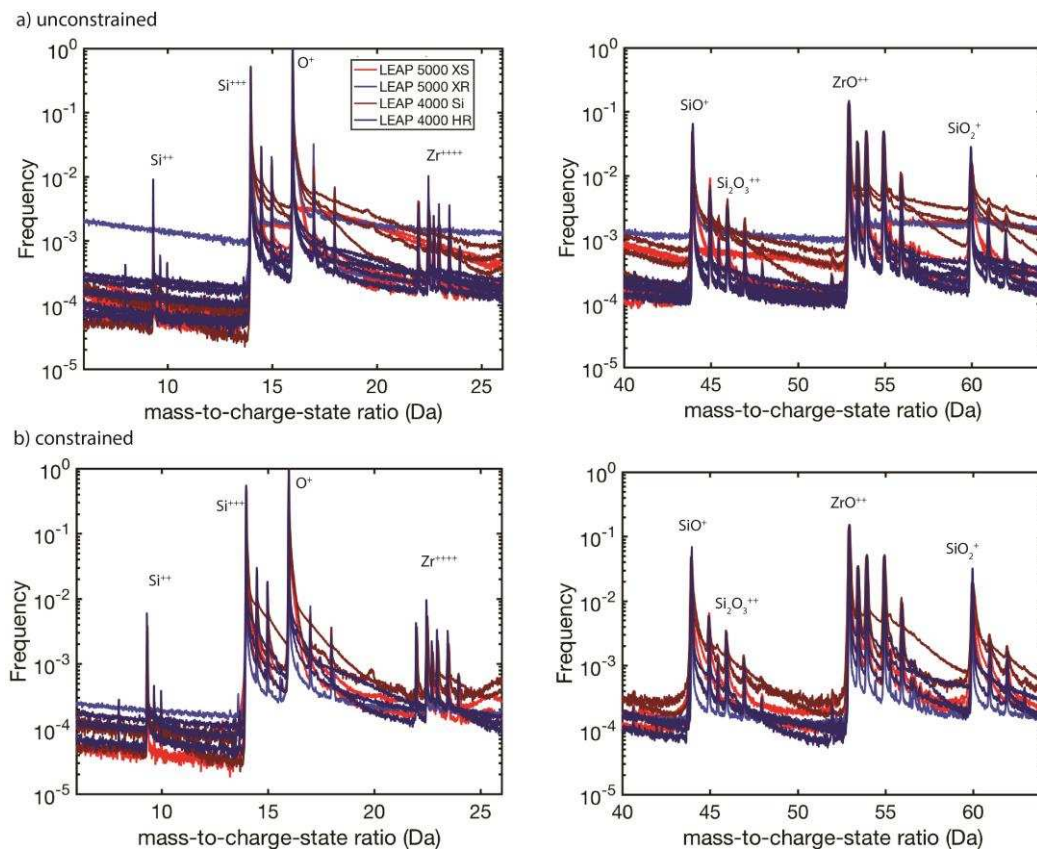


Figure 7: Normalized mass spectra for both unconstrained and constrained rounds.

A more quantitative way to compare mass spectra from different origins is to look at the signal-to-background ratio for a selected peak versus charge-state-ratio (which gives an indication of the field intensity) or background level around the H peak (informing on the vacuum state of the instrument). Here the signal-to-background ratios were measured for the Y^{+++} peak, which corresponds to one of the major trace elements within the zircon under investigation. Y^{+++} was detected by most of the participants at a level of ~ 200 ppma on average (close to the level detected by LAICPMS (197 ppmw)). As shown in the inset in **Figure 8** (b), the peak position in the mass spectrum, at 29.66 Da, is clear of major thermal tails or isobaric overlaps. It is plotted against the charge-state-ratio of ZrO ($ZrO^{3+}/(ZrO^{3+} + ZrO^{2+})$) in order to reflect the field intensity (**Figure 8** (a)). The charge-state-ratio of a peak has previously been shown to qualitatively reflect the intensity of the field, [53, 54] where a higher charge-state-ratio corresponds to higher field. The ZrO species was chosen for its abundance and the absence of isobaric interference at the position of its two molecular ions, ZrO^{3+} and ZrO^{2+} .

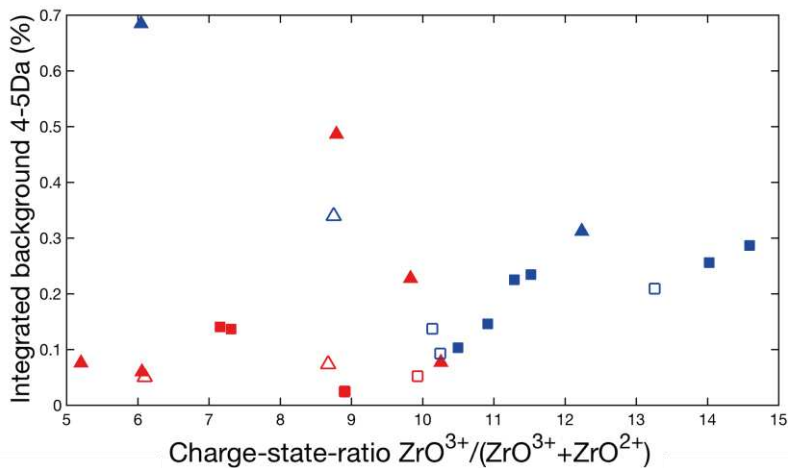
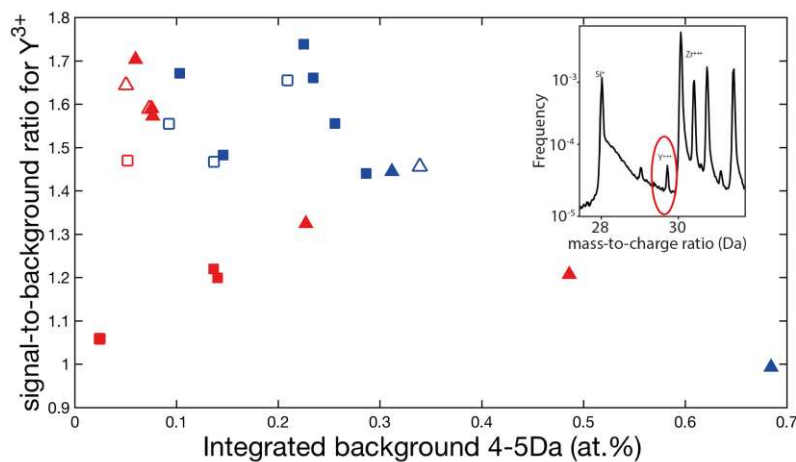
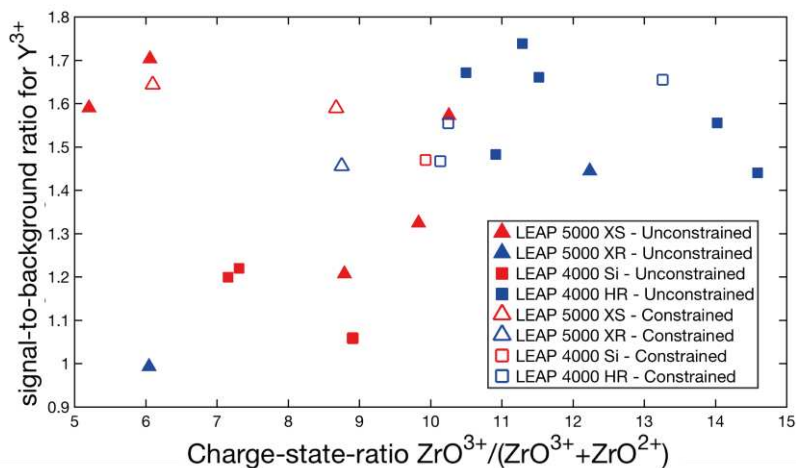


Figure 8: Measures of background noise and their dependence on the evaporation field, as indicated by the ZrO charge state ratio

Interestingly, the signal-to-background ratios are higher for the reflectron-fitted systems and also display less dispersion than for the straight flight path instruments (**Figure 8** (a) and (b)). This likely originates from the slightly better mass resolution of the spectra from reflectron-fitted instruments (blue in **Figure 7**). The electric field is also more intense in the case of reflectron-fitted systems. This can be explained by a lower detection efficiency as well as a

smaller field of view for these systems. In order to sustain an equivalent detection rate, experiments performed with reflectron-fitted systems will require a higher evaporation field compared to a straight flight path system. Note that the field can be lowered with a higher laser pulse energy or lower detection rate. The level of background is also slightly higher with a more intense field, but this seems to have a limited impact on the signal-to-background ratios (**Figure 8** (b) and (c)). While the instrument model (4000 vs 5000) does not appear to play a role in the mass spectra quality, there is some improvement in signal-to-background ratios with reflectron-fitted systems.

4. Conclusions

The variation in the measured composition across this round robin study highlights the need to provide guidelines and/or standards for the APT study of specific types of materials. This study confirms the importance of the user's choice in identifying and ranging peaks. The local ranged-assisted background model used by most of the participants is thought to be a good fit for such complicated mass spectra and as a result should be a standard correction for APT of zircons. The dispersion of parameters used by our participants to analyze and reconstruct the zircon GJ-1/87 reflects the multiple factors that influence an APT experiment, posing a challenge for the standardization of APT experimental protocols. The type of instrument has a small influence on the data acquired, hence does not seem the most critical factor. Interestingly, in this study, the experiments were performed at higher fields in the reflectron-fitted instruments due to the detection efficiency being lower. Reflectron systems yield slightly better signal-to-background ratios for the selected Y peak examined in this paper. Values of the laser pulse energy or parameters that relate to the specimen geometry are too difficult to control or to be reproduced, and only parameters from the analysis itself should be considered. The background has a strong influence, and better ways to quantify this may be needed. Finally, the charge state ratios seem an interesting parameter to use for APT data comparison as it can be monitored during the course of the analysis and is only dependent on the physics of the field evaporation.

REFERENCES

- [1] E.A. Marquis, V. Araullo-Peters, A. Etienne, S. Fedotova, K. Fujii, K. Fukuya, E. Kuleshova, A. Legrand, A. London, S. Lozano-Perez, Y. Nagai, K. Nishida, B. Radiguet, D. Schreiber, N. Soneda, M. Thuvander, T. Toyama, F. Sefta, P. Chou, A Round Robin Experiment: Analysis of Solute Clustering from Atom Probe Tomography Data, *Microscopy and Microanalysis* 22(S3) (2016) 666-667.
- [2] J. MacDonald, Zircon—Earth's timekeeper, *Geology Today* 29(3) (2013) 113-117.
- [3] A. Möller, P. O'Brien, A. Kennedy, A. Kröner, Polyphase zircon in ultrahigh - temperature granulites (Rogaland, SW Norway): Constraints for Pb diffusion in zircon, *Journal of metamorphic Geology* 20(8) (2002) 727-740.
- [4] D. Cherniak, J. Hanchar, E. Watson, Rare-earth diffusion in zircon, *Chemical Geology* 134(4) (1997) 289-301.
- [5] D.J. Cherniak, E.B. Watson, Diffusion in zircon, *Reviews in mineralogy and geochemistry* 53(1) (2003) 113-143.
- [6] P.W.O. Hoskin, U. Schaltegger, The Composition of Zircon and Igneous and Metamorphic Petrogenesis, *Reviews in Mineralogy and Geochemistry* 53(1) (2003) 27-62.
- [7] A. Radionova, I. Filippov, P.J. Derrick, In pursuit of resolution in time - of - flight mass spectrometry: A historical perspective, *Mass spectrometry reviews* (2015).
- [8] S.M. Reddy, N.E. Timms, P. Trimby, P.D. Kinny, C. Buchan, K. Blake, Crystal-plastic deformation of zircon: A defect in the assumption of chemical robustness, *Geology* 34(4) (2006) 257-260.
- [9] S.M. Reddy, N.E. Timms, W. Pantleon, P. Trimby, Quantitative characterization of plastic deformation of zircon and geological implications, *Contributions to Mineralogy and Petrology* 153(6) (2007) 625-645.
- [10] S.M. Reddy, N.E. Timms, P.J. Hamilton, H.R. Smyth, Deformation-related microstructures in magmatic zircon and implications for diffusion, *Contributions to Mineralogy and Petrology* 157(2) (2009) 231-244.
- [11] S. Piazzolo, H. Austrheim, M. Whitehouse, Brittle-ductile microfabrics in naturally deformed zircon: Deformation mechanisms and consequences for U-Pb dating, *American Mineralogist* 97(10) (2012) 1544-1563.
- [12] N.E. Timms, P.D. Kinny, S.M. Reddy, Enhanced diffusion of uranium and thorium linked to crystal plasticity in zircon, *Geochemical Transactions* 7(1) (2006) 10.
- [13] M.A. Kusiak, M.J. Whitehouse, S.A. Wilde, D.J. Dunkley, M. Menneken, A.A. Nemchin, C. Clark, Changes in zircon chemistry during Archean UHT metamorphism in the Napier Complex, Antarctica, *American Journal of Science* 313(9) (2013) 933-967.
- [14] E. Kovaleva, U. Klötzli, G. Habler, J. Wheeler, Planar microstructures in zircon from paleo-seismic zones, *American Mineralogist* 100(8-9) (2015) 1834-1847.
- [15] S.L. Harley, L.P. Black, A revised Archean chronology for the Napier Complex, Enderby Land, from SHRIMP ion-microprobe studies, *Antarctic Science* 9(1) (2004) 74-91.
- [16] M. Petrelli, K. Laeger, D. Perugini, High spatial resolution trace element determination of geological samples by laser ablation quadrupole plasma mass spectrometry: implications for glass analysis in volcanic products, *Geosciences Journal* 20(6) (2016) 851-863.
- [17] M.R. Kilburn, D. Wacey, Chapter 1 Nanoscale Secondary Ion Mass Spectrometry (NanoSIMS) as an Analytical Tool in the Geosciences, *Principles and Practice of Analytical Techniques in Geosciences*, The Royal Society of Chemistry 2015, pp. 1-34.
- [18] M.A. Kusiak, M.J. Whitehouse, S.A. Wilde, A.A. Nemchin, C. Clark, Mobilization of radiogenic Pb in zircon revealed by ion imaging: Implications for early Earth geochronology, *Geology* 41(3) (2013) 291-294.

- [19] B. Gault, M.P. Moody, J.M. Cairney, S.P. Ringer, Atom probe microscopy, Springer 2012.
- [20] D.J. Larson, T.J. Prosa, R.M. Ulfing, B.P. Geiser, T.F. Kelly, Local electrode atom probe tomography, New York, US: Springer Science (2013).
- [21] J.W. Valley, A.J. Cavosie, T. Ushikubo, D.A. Reinhard, D.F. Lawrence, D.J. Larson, P.H. Clifton, T.F. Kelly, S.A. Wilde, D.E. Moser, Hadean age for a post-magma-ocean zircon confirmed by atom-probe tomography, *Nature Geoscience* 7(3) (2014) 219-223.
- [22] S. Piazzolo, A. La Fontaine, P. Trimby, S. Harley, L. Yang, R. Armstrong, J.M. Cairney, Deformation-induced trace element redistribution in zircon revealed using atom probe tomography, *Nature communications* 7 (2016).
- [23] E.M. Peterman, S.M. Reddy, D.W. Saxey, D.R. Snoeyenbos, W.D. Rickard, D. Fougereuse, A.R. Kylander-Clark, Nanogeochronology of discordant zircon measured by atom probe microscopy of Pb-enriched dislocation loops, *Science Advances* 2(9) (2016) e1601318.
- [24] A. La Fontaine, S. Piazzolo, P. Trimby, L. Yang, J.M. Cairney, Laser-Assisted Atom Probe Tomography of Deformed Minerals: A Zircon Case Study, *Microscopy and Microanalysis* (2017) 1-10.
- [25] S.M. Reddy, A. van Riessen, D.W. Saxey, T.E. Johnson, W.D. Rickard, D. Fougereuse, S. Fischer, T.J. Prosa, K.P. Rice, D.A. Reinhard, Mechanisms of deformation-induced trace element migration in zircon resolved by atom probe and correlative microscopy, *Geochimica et Cosmochimica Acta* 195 (2016) 158-170.
- [26] P. Panayi, Atom probe, Google Patents, 2007.
- [27] P. Clifton, T. Gribb, S. Gerstl, R.M. Ulfing, D.J. Larson, Performance Advantages of a Modern, Ultra-High Mass Resolution Atom Probe, *Microscopy and Microanalysis* 14(S2) (2008) 454-455.
- [28] K. Kuhlman, R. Martens, T. Kelly, N. Evans, M. Miller, Fabrication of specimens of metamorphic magnetite crystals for field ion microscopy and atom probe microanalysis, *Ultramicroscopy* 89(1) (2001) 169-176.
- [29] M. Miller, K. Russell, An APFIM investigation of a weathered region of the Santa Catharina meteorite, *Surface science* 266(1-3) (1992) 441-445.
- [30] P.R. Heck, F.J. Stadermann, D. Isheim, O. Auciello, T.L. Daulton, A.M. Davis, J.W. Elam, C. Floss, J. Hiller, D.J. Larson, Atom - probe analyses of nanodiamonds from Allende, *Meteoritics & Planetary Science* 49(3) (2014) 453-467.
- [31] M. Miller, G. Smith, An atom probe study of the anomalous field evaporation of alloys containing silicon, *Journal of Vacuum Science and Technology* 19(1) (1981) 57-62.
- [32] T. Hashizume, Y. Hasegawa, A. Kobayashi, T. Sakurai, Atom - probe investigation of III - V semiconductors: Comparison of voltage - pulse and laser - pulse modes, *Review of scientific instruments* 57(7) (1986) 1378-1380.
- [33] M. Müller, B. Gault, G. Smith, C. Grovenor, Accuracy of pulsed laser atom probe tomography for compound semiconductor analysis, *Journal of Physics: Conference Series*, IOP Publishing, 2011, p. 012031.
- [34] D. Saxey, Correlated ion analysis and the interpretation of atom probe mass spectra, *Ultramicroscopy* 111(6) (2011) 473-479.
- [35] D. Santhanagopalan, D.K. Schreiber, D.E. Perea, R.L. Martens, Y. Janssen, P. Khalifah, Y.S. Meng, Effects of laser energy and wavelength on the analysis of LiFePO₄ using laser assisted atom probe tomography, *Ultramicroscopy* 148 (2015) 57-66.
- [36] L. Mancini, N. Amirifar, D. Shinde, I. Blum, M. Gilbert, A. Vella, F. Vurpillot, W. Lefebvre, R. Lardé, E. Talbot, Composition of wide bandgap semiconductor materials and nanostructures measured by atom probe tomography and its dependence on the surface electric field, *The Journal of Physical Chemistry C* 118(41) (2014) 24136-24151.
- [37] B. Gault, D.W. Saxey, M.W. Ashton, S.B. Sinnott, A.N. Chiaramonti, M.P. Moody, D.K. Schreiber, Behavior of molecules and molecular ions near a field emitter This work is a partial

contribution of the US Government and therefore is not subject to copyright in the United States, *New Journal of Physics* 18(3) (2016) 033031.

[38] I. Blum, L. Rigutti, F. Vurpillot, A. Vella, A. Gaillard, B. Deconihout, Dissociation dynamics of molecular ions in high DC electric field, *The Journal of Physical Chemistry A* 120(20) (2016) 3654-3662.

[39] F. Tang, B. Gault, S.P. Ringer, J.M. Cairney, Optimization of pulsed laser atom probe (PLAP) for the analysis of nanocomposite Ti–Si–N films, *Ultramicroscopy* 110(7) (2010) 836-843.

[40] L. Yao, J. Cairney, C. Zhu, S. Ringer, Optimisation of specimen temperature and pulse fraction in atom probe microscopy experiments on a microalloyed steel, *Ultramicroscopy* 111(6) (2011) 648-651.

[41] G.D. Costa, H. Wang, S. Duguay, A. Bostel, D. Blavette, B. Deconihout, Advance in multi-hit detection and quantization in atom probe tomography, *Review of Scientific Instruments* 83(12) (2012) 123709.

[42] E. Belousova, Y. Kostitsyn, W.L. Griffin, G.C. Begg, S.Y. O'Reilly, N.J. Pearson, The growth of the continental crust: constraints from zircon Hf-isotope data, *Lithos* 119(3) (2010) 457-466.

[43] S. Piazzolo, E. Belousova, A. La Fontaine, C. Corcoran, J.M. Cairney, Trace element homogeneity from micron-to atomic scale: Implication for the suitability of the zircon GJ-1 as a trace element reference material, *Chemical Geology* (2017).

[44] A.J. Melmed, J.J. Carroll, S.S. Brenner, Round-robin atom-probe experiment: Preliminary results, *Ultramicroscopy* 4(3) (1979) 386.

[45] S. Nakamura, Round-robin atom probe experiment: preliminary results in Japan *Le Journal de Physique Colloques* 47(C2) (1986) C2-459-C2-464.

[46] D. Hudson, G. Smith, B. Gault, Optimisation of mass ranging for atom probe microanalysis and application to the corrosion processes in Zr alloys, *Ultramicroscopy* 111(6) (2011) 480-486.

[47] D. Arvizu, P. Balaya, L. Cabeza, T. Hollands, A. Jäger-Waldau, M. Kondo, C. Konseibo, V. Meleshko, W. Stein, Y. Tamaura, H. Xu, R. Zilles, 2011: Direct Solar Energy. In IPCC Special Report on Renewable Energy Sources and Climate Change Mitigation [O. Edenhofer, R. Pichs-Madruga, Y. Sokona, K. Seyboth, P. Matschoss, S. Kadner, T. Zwickel, P. Eickemeier, G. Hansen, S. Schlömer, C. von Stechow (eds), (2011).

[48] J.T. Sebastian, O.C. Hellman, D.N. Seidman, New method for the calibration of three-dimensional atom-probe mass spectra, *Review of Scientific Instruments* 72(7) (2001) 2984-2988.

[49] *Cameca, IVAS™ 3.6.6 User Guide*, 2013.

[50] B. Geiser, D. Larson, E. Oltman, S. Gerstl, D. Reinhard, T. Kelly, T. Prosa, Wide-field-of-view atom probe reconstruction, *Microscopy and Microanalysis* 15(S2) (2009) 292-293.

[51] P. Bas, A. Bostel, B. Deconihout, D. Blavette, A general protocol for the reconstruction of 3D atom probe data, *Applied Surface Science* 87 (1995) 298-304.

[52] B. Gault, D. Haley, F. De Geuser, M. Moody, E. Marquis, D. Larson, B. Geiser, Advances in the reconstruction of atom probe tomography data, *Ultramicroscopy* 111(6) (2011) 448-457.

[53] D.R. Kingham, Charge state of ions in liquid metal field ion sources, *Applied Physics A* 31(3) (1983) 161-164.

[54] D.K. Schreiber, A.N. Chiaramonti, L.M. Gordon, K. Kruska, Applicability of post-ionization theory to laser-assisted field evaporation of magnetite, *Applied Physics Letters* 105(24) (2014) 244106.

SUPPLEMENTARY

Analysis	Al	P	Ti	Cu	Ga	Ge	As	Rb	Y	Nb	Hf	Ta	Pb	Th	U
GJ-87-01	5.35	34.0	4.63	0.12	0.43	<0.15	0.213	0.06	197	2.02	5563	0.50	76.6	14.1	222
GJ-87-02	5.43	29.0	4.42	0.07	0.45	<0.14	<0.15	0.08	198	2.02	5567	0.49	77.0	14.3	223
GJ-87-03	5.37	30.8	4.13	0.10	0.43	0.19	0.22	0.08	200	2.02	5573	0.48	75.6	14.4	216
GJ-87-04	5.38	29.7	4.64	0.08	0.44	<0.14	<0.15	0.05	202	2.00	5600	0.48	74.2	14.1	212
GJ-87-05	5.26	30.6	4.55	0.10	0.46	0.14	0.23	0.06	198	2.02	5546	0.46	75.1	14.1	215
GJ-87-06	5.27	30.6	4.45	0.10	0.43	<0.13	0.21	0.05	195	1.99	5541	0.49	76.0	14.2	221
GJ-87-07	5.28	28.5	4.34	0.08	0.43	0.17	<0.12	0.07	195	1.96	5549	0.48	73.5	13.8	213
GJ-87-08	5.41	32.2	4.95	0.11	0.46	0.21	0.15	0.06	196	2.00	5483	0.46	79.6	14.1	230
GJ-87-09	5.54	27.4	4.67	0.11	0.46	0.16	<0.12	0.05	192	1.97	5458	0.48	79.3	14.1	230
GJ-87-10	5.59	31.9	4.34	0.08	0.46	<0.12	0.23	0.06	192	2.06	5473	0.46	82.6	13.7	233
Average	5.38	30.5	4.51	0.10	0.45	0.18	0.21	0.06	197	2.01	5535	0.48	76.9	14.1	222
1SD	0.11	1.93	0.22	0.01	0.01	0.02	0.03	0.01	3.2	0.03	47	0.01	2.8	0.2	7.7
1σ	0.21	3.0	0.23	0.01	0.02	0.05	0.05	0.01	6.7	0.07	186	0.02	3.3	0.5	8.4
RSD%	3.9	9.8	5.1	10	4.9	28	24	14	3.4	3.7	3.4	3.8	4.2	3.9	3.8

Analysis	La	Ce	Pr	Nd	Sm	Eu	Gd	Tb	Dy	Ho	Er	Tm	Yb	Lu
GJ-87-01	0.002	15.2	0.03	0.66	1.46	0.84	5.44	1.55	17.2	5.55	23.7	5.49	58.0	9.04
GJ-87-02	0.002	15.3	0.03	0.65	1.47	0.91	5.38	1.59	17.3	5.59	23.8	5.46	58.7	9.03
GJ-87-03	0.001	15.0	0.03	0.72	1.50	0.87	5.48	1.64	17.2	5.59	24.2	5.52	57.7	9.2
GJ-87-04	0.002	14.8	0.03	0.72	1.48	0.87	5.54	1.61	17.7	5.68	24.2	5.54	57.9	9.15
GJ-87-05	0.001	14.9	0.02	0.72	1.46	0.89	5.56	1.6	17.2	5.55	23.8	5.39	57.8	9.06
GJ-87-06	0.001	15.2	0.03	0.69	1.43	0.87	5.61	1.61	17.5	5.53	23.4	5.45	58.0	8.93
GJ-87-07	<0.001	14.7	0.03	0.70	1.54	0.90	5.55	1.55	17.2	5.46	23.4	5.49	57.2	8.87
GJ-87-08	<0.002	15.5	0.04	0.72	1.50	0.92	5.65	1.59	17.2	5.54	23.7	5.41	59.1	8.95
GJ-87-09	<0.001	15.6	0.03	0.72	1.58	0.89	5.68	1.57	17.3	5.53	23.3	5.42	59.3	8.77
GJ-87-10	<0.002	15.2	0.03	0.73	1.50	0.91	5.48	1.57	17.1	5.51	23.3	5.43	58.8	8.78
Average	0.002	15.2	0.03	0.71	1.51	0.89	5.53	1.59	17.3	5.55	23.7	5.46	58.3	8.98
1SD	0.001	0.3	0.003	0.028	0.04	0.02	0.09	0.02	0.2	0.05	0.34	0.05	0.70	0.14
1σ^a	0.001	0.64	0.002	0.03	0.06	0.03	0.23	0.05	0.6	0.18	0.83	0.18	2.1	0.30
RSD%	48	4.2	7.5	4.8	4.1	4.1	4.2	3.6	3.4	3.3	3.5	3.4	3.5	3.3

^a 1 σ calculated using GLITTER 2008.

Table S1 LA-ICPMS data (ppm) for the GJ-1/87 zircon standard.

Symbol	Temperature (K)	Laser energy (μJ)	Laser pulse (kHz)	Detection rate (%)
5S-I	50	100	250	2
5S-II	40	500	250	1
	30	700	250	1
5R-I	55	100	125	1
5R-II	50	175	Variable	0.5
5S-III	50	175	Variable	0.5
4R-I	54.7	100	200	0.8
	54.7	100	200	0.7
4R-II	59.7	350	200	0.75
	59.7	250	125	0.5
4S-I	54.7	100	200	0.7
	57.3	400	200	0.5
4S-II	50	300	250	0.5
4R-III	50	400	250	0.5

Symbol	Evaporation Field (V/nm)	Atomic volume (nm^3/atom)	k-factor	ICF	Detector Efficiency (%)	Radius evolution	Background model
5S-I	Tip profile reconstruction method was used (initial radius: 151.58 nm; final radius: 156.475; tip length: 75.855)				80		Local-mass
5S-II	28 (Zr)	0.0233 (Zr)	3.3	1.65	80	Shank (1.7 deg.)	Local-ranged
	28 (Zr)	0.0233 (Zr)	3.3	1.65	80	Shank (1.7 deg.)	Local-ranged
5R-I	28 (Zr)	0.0233 (Zr)	3.3	1.65	52	Voltage	Local-ranged
5R-II	25	0.010912	3.3	1.03	80	Voltage	Local-ranged
5S-III	25	0.010912	3.3	1.03	80	Voltage	Local-ranged
4R-I	32	0.01076	3.3	1.65	37	Voltage	Local-ranged
	32	0.01076	3.3	1.65	37	Voltage	Local-ranged
4R-II	28 (Zr)	0.0233 (Zr)	2.6	1.65	36	Voltage	Local-ranged
	28 (Zr)	0.0233 (Zr)	2.6	1.65	36	Shank (4.44 deg.)	Local-ranged
4S-I	28 (Zr)	0.0233 (Zr)	2.6	1.65		unknown	In-house
	28 (Zr)	0.0233 (Zr)	2.6	1.65			In-house
4S-II	32	0.010076	3.3	1.65	57	Voltage	Local-ranged
4R-III	28 (Zr)	0.0233 (Zr)	3.3	1.65	36	Voltage	Local-ranged

Table S2 Acquisition and reconstruction parameters for unconstrained and constrained rounds.

unconstrained	O	Zr	Si	Hf	Y
	at %	at %	at %	ppma	ppma
5S-I	64.8 ±0.02	18.7 ±0.01	16.4 ±0.01	1840 ±7.37	126 ±1.93
5S-II	62.66 ±0.01	20.14 ±0.01	16.97 ±0.01	1126.75 ±100	191.81 ±100
	62.66 ±0.01	20.14 ±0.01	16.97 ±0.01	1070.79 ±5.58	232.57 ±2.6
5R-I	61.80 ±0.01	18.58 ±0.01	15.40 ±0.01	1125.12 ±4.30	
5R-II	67.45 ±0.03	16.63 ±0.02	15.71 ±0.02	1155.04 ±22.19	98.23 ±12.37
	69.12 ±0.02	15.40 ±0.01	15.28 ±0.01	1180.20 ±16.97	106.39 ±9.42
5S-III	70.83 ±0.05	14.61 ±0.02	14.36 ±0.02	1283.34 ±58.13	
4R-I	62.51 ±0.02	18.44 ±0.01	17.13 ±0.01	1030.77 ±7.05	52.51 ±1.59
	62.23 ±0.02	18.16 ±0.01	17.13 ±0.01	1021.05 ±7.06	60.21 ±1.71
4R-II	63.67 ±0.01	19.00 ±0.01	17.23 ±0.01	969.42 ±6.93	
	63.76 ±0.01	18.96 ±0.01	17.19 ±0.01	900.29 ±7.15	
4S-I	69.07 ±0.05	15.93 ±0.02	14.84 ±0.02	871.48 ±20.13	56.79 ±7.58
	66.92 ±0.04	17.23 ±0.02	15.68 ±0.01	894.18 ±15.11	54.91 ±5.56
4S-II	69.61 ±0.02	15.14 ±0.01	15.13 ±0.01	829.53 ±6.54	50.53 ±1.61
4R-III	63.38 ±0.01	19.08 ±0.01	17.41 ±0.01	1210.00 ±10.00	90.00 ±10.00
	63.24 ±0.01	19.16 ±0.01	17.48 ±0.01	1110.00 ±10.00	70.00 ±10.00

constrained	O	Zr	Si	Hf	Y
	at %	at %	at %	ppma	ppma
5S-I	63.80 ±0.02	19.60 ±0.01	16.40 ±0.01	1490.00 ±7.76	117.00 ±2.17
5S-II	63.35 ±0.01	19.75 ±0.01	16.60 ±0.01	1293.29 ±100.00	198.72 ±100.00
5R-I	67.53 ±0.01	16.83 ±0.01	15.56 ±0.01	806.41 ±2.08	
4R-I	62.95 ±0.02	16.96 ±0.01	18.12 ±0.01	841.97 ±5.60	38.59 ±1.20
4R-II	64.87 ±0.00	18.02 ±0.00	17.02 ±0.00	912.25 ±0.69	
4S-I	64.34 ±0.04	19.20 ±0.02	16.29 ±0.01	1059.70 ±21.16	70.91 ±5.95
4S-II	69.61 ±0.02	15.14 ±0.01	15.13 ±0.01	829.53 ±6.54	50.53 ±1.61
4R-III	63.42 ±0.01	19.08 ±0.01	17.37 ±0.01	1210.00 ±10.00	70.00 ±10.00

Ranging	O	Zr	Si	Hf	Y
	at %	at %	at %	ppma	ppma
5S-I	64.39 ±0.01	20.60 ±0.01	14.89 ±0.01	1036.30 ±4.59	204.37 ±2.04
5S-II	67.33 ±0.01	16.70 ±0.01	13.26 ±0.01	823.19 ±5.39	1389.86 ±63.69
5R-I	67.53 ±0.01	16.83 ±0.01	15.56 ±0.01	806.41 ±2.08	
5R-II	66.11 ±0.01	16.70 ±0.01	17.09 ±0.01	771.40 ±8.73	58.76 ±3.80
4R-I	62.61 ±0.02	20.55 ±0.01	16.41 ±0.01	929.29 ±4.61	40.83 ±0.97
4R-II	67.51 ±0.01	16.59 ±0.01	15.82 ±0.01	849.07 ±5.46	
4S-I	68.52 ±0.03	15.75 ±0.01	15.59 ±0.01	849.70 ±11.91	53.99 ±3.94
4S-II	67.59 ±0.02	17.36 ±0.01	14.65 ±0.01	1739.44 ±7.94	68.20 ±7.13
4R-III	67.50 ±0.01	16.57 ±0.01	15.84 ±0.01	820.00 ±10.00	100.00 ±10.00

Table S3 Composition of O, Zr, Si, Hf and Y measured by APT for the three rounds.

unconstrained	Er	Th	Nb	P	U	Cr
	ppma	ppma	ppma	ppma	ppma	ppma
5S-II		54.43 ±10	70.59 ±10		298.81 ±100	460.42 ±10
		122.62 ±1.89	105.34 ±1.75		332.85 ±3.11	444.41 ±3.59
5R-II	41.82 ±7.08	99.50 ±7.70	159.64 ±18.11	70.63 ±9.30	11.62 ±5.47	11.62 ±5.47
	36.82 ±5.36	52.64 ±5.79	158.58 ±13.92	81.32 ±7.24	52.76 ±9.24	52.76 ±9.24
5S-III			195.22 ±21.51	114.39 ±18.01		
4S-I	664.05 ±40.99 608.77 ±29.98					
4S-II	22.80 ±1.08	9.51 ±0.70		47.99 ±1.57		

	Sc	C	Dy	Li	Al	Tm	Ta
	ppma	ppma	ppma	ppma	ppma	ppma	ppma
5S-II		109.08 ±10		15.08 ±10	32.46 ±10		
		83.74 ±1.56		40.27 ±1.08	17.37 ±0.71		
5R-II	289.55 ±7.25		84.08 ±6.83			14.32 ±6.92	13.67 ±5.47
	230.28 ±5.24		61.93 ±5.17			21.96 ±4.66	16.24 ±4.07
5S-III	406.76 ±15.56						

constrained	Th	Er	U	Nb
	ppma	ppma	ppma	ppma
5S-II	614.30 ±10.00		595.68 ±10.00	128.22 ±10.00
4S-I		544.42 ±23.81		
4S-II	9.51 ±0.70	22.80 ±1.08		

	Cr	C	P	Al	Li
	ppma	ppma	ppma	ppma	ppma
5S-II	64.23 ±10.00	57.01 ±10.00		48.50 ±10.00	11.28 ±10.00
4S-I					
4S-II			47.99 ±1.57		

ranging	Er	N	U	P	Cr
	ppma	ppma	ppma	ppma	ppma
5S-II		23360.39 ±28.36	66.55 ±6.96		1375.55 ±6.96
5R-II	33.95 ±2.12			50.96 ±5.96	
4S-I	490.79 ±24.83				

	Th	Dy	W	Tm
	ppma	ppma	ppma	ppma
5S-II	25.55 ±6.96		63.42 ±6.96	
5R-II		31.95 ±2.21		14.53 ±2.48
4S-I				

Table S4 Composition of minor trace elements measured by APT for the three rounds.